Journal of The Electrochemical Society, **154** (11) B1158-B1166 (2007)
0013-4651/2007/154(11)/B1158/9/$20.00 © The Electrochemical Society

Gas Purge in a Polymer Electrolyte Fuel Cell

Puneet K. Sinha* and **Chao-Yang Wang****,z**

Electrochemical Engine Center (ECEC) and Department of Mechanical and Nuclear Engineering, The Pennsylvania State University, University Park, Pennsylvania 16802, USA

Gas purge intended to minimize residual water in the membrane, porous electrodes, and gas diffusion layers is critical for successful start-up of a polymer electrolyte fuel cell (PEFC) from subfreezing temperatures. A basic understanding of the physical phenomena involved in gas purge, required to establish effective and energy-saving purge protocols, is necessary. In this work, we present a physical model describing water removal from a PEFC during gas purge. Various stages of gas diffusion layer (GDL) and membrane drying are characterized, and the variations along the flow direction are considered and emphasized. The predicted GDL drying time constant is compared to the tomographic experiments with good agreement. The effect of purge conditions on purge effectiveness is elucidated. It is found that low relative humidity of purge gas, high gas flow rate, and high cell temperature favor effective purge.
 [DOI: 10.1149/1.2776226]

Manuscript submitted May 25, 2007; revised manuscript received July 2, 2007. Available electronically September 13, 2007.

Extensive worldwide efforts are steadily driving fuel cell technology toward the goal of a sustainable and clean energy future. At present, cold start capability and survivability of a polymer electrolyte fuel cell (PEFC) is among the remaining major challenges in realizing PEFC technology for automotive applications. To date, only a few yet significant efforts have been made to reveal the fundamental mechanism of cold start.[1-6] It is recognized that product water becomes frost or ice on start-up when the cell temperature is below the freezing point of water. The product water created in a subzero environment may diffuse into the membrane if it is dry, initially, or otherwise precipitates as ice or frost in the cathode catalyst layer (CL), leading to CL plugging by solid water and PEFC shutdown before the cell temperature rises above freezing. It thus follows that a drier membrane prior to cold start facilitates cold start with longer operation time. More commonly, gas purge is performed for control and minimization of residual water in a PEFC prior to engine shutdown. Minimal residual water ensued by gas purge further lessens the degradation of cell performance during freeze/thaw cycles.[7]

A fundamental understanding of gas purge is warranted not only because it sets up the initial water distribution for cold start but also due to the stringent requirement of short purge duration for practical convenience and energy conservation in a vehicle. In this context, we define the "purge effectiveness" such that the membrane high-frequency resistance (HFR) reaches a certain high value in the shortest time, noting that membrane HFR is a direct measure of membrane hydration.

Numerical and experimental investigations for a basic understanding of gas purge are scarce in the literature. Bradean et al.[8] showed, based on a one-dimensional (1D) purge model, that the cell temperature is the most sensitive parameter controlling purge effectiveness. However, no efforts were made to characterize the underlying physics of gas purge. Ge and Wang[6] measured the membrane HFR as a function of purge time and correlated HFR increase with the presence of liquid water in CL and GDL. Sinha et al.[9] measured liquid water removal from GDL by purge gas using X-ray microtomography. They showed that purge gas erodes liquid water clusters in the GDL, giving birth to small isolated clusters that can be removed only by evaporation, resulting in exponential decay in drying rate. Similar conclusions were made in studies,[10-14] investigating drying of general porous media, an analogous problem to gas purge in a PEFC. Using pore-network models, Prat,[10,11] Laurindo and Prat,[12] and Bray and Prat[13] were the first to theoretically characterize drying patterns and their rate of change in hydrophilic porous structures. Taking detailed pore-level mechanisms into account, Laurindo and Prat[12] explained that the drying process consists of an initial fast drying rate period followed by a significantly slower rate period. The fast rate period is a result of viscous pressure gradient-driven liquid flow to the evaporation front, whereas the slow rate period is a result of evaporation of poorly connected liquid islands that are unable to sustain continuous liquid flow. Yortsos et al.[15,16] further delineated the role of wetting liquid film in drying, formed along the rough edges and corners of pores, and showed that wetting films significantly increases drying rate. Segura and Toledo[17] computed relative permeability of liquid and gas phases during drying.

In parallel to these pore-scale investigations, macroscopic models have been proposed in the past few decades to investigate convective drying of porous media for applications ranging from soil science to food processing. These models have either adopted Luikov's phenomenological approach,[18] using thermodynamics theory of irreversible processes to describe the temperature, moisture, and pressure distributions in a porous medium during drying, or Whitaker's volume averaging method.[19] A majority of models[20-25] follow Whitaker's approach and thus treat convective drying as a classical problem of coupled heat and mass transfer in porous media. At the macroscale, drying is further divided into the funicular stage in which liquid transport due to capillary flow is dominant and the pendular stage where moisture movement is solely driven by vapor diffusion. Funicular and pendular stages are distinguished at the onset of irreducible liquid saturation in several macroscopic models.[26,27] The two-phase Darcy's law is generally used to investigate the funicular stage, whereas over the years several modifications have been proposed to address liquid phase removal in the pendular stage: liquid phase removal due to evaporation only,[28] incorporation of liquid transport through liquid films along the corners,[29] and mass transfer due to chemical potential gradient,[30] to name a few. Additionally, drying in a hydrophobic porous medium has been scarcely researched. Most recently, Shahidzadeh-Bonn et al.[31] investigated the effect of wetting properties on drying and showed substantial differences in drying rates of hydrophilic and hydrophobic porous media. However, no efforts have been made to elucidate the governing physics of drying in a hydrophobic medium.

Although gas purge in a PEFC is analogous to convective drying of a porous medium, substantial differences exist, such as liquid water being a nonwetting phase in a hydrophobic GDL, thin layers of GDL ($\sim$200 μm), CL ($\sim$10 μm), and membrane (10–50 μm), the presence of current-collecting lands obstructing water removal, and the presence of ionomer in CL and membrane. In this article, we develop a fundamental understanding of gas purge characteristics and a first purge model. The article is organized as follows: a detailed description of the governing physics of gas purge is presented along with characterization of various stages. Subsequently, an analysis is developed to predict each stage of purge, yielding a

* Electrochemical Society Student Member.
** Electrochemical Society Active Member.
z E-mail: cxw31@psu.edu

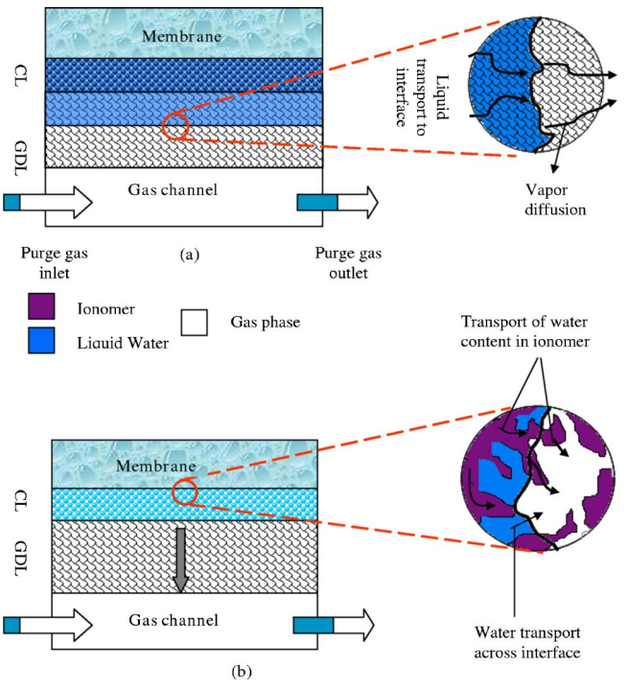

Figure 1. (Color online) Schematic representation of physics in gas purge: (a) GDL drying and (b) membrane and catalyst layer drying.

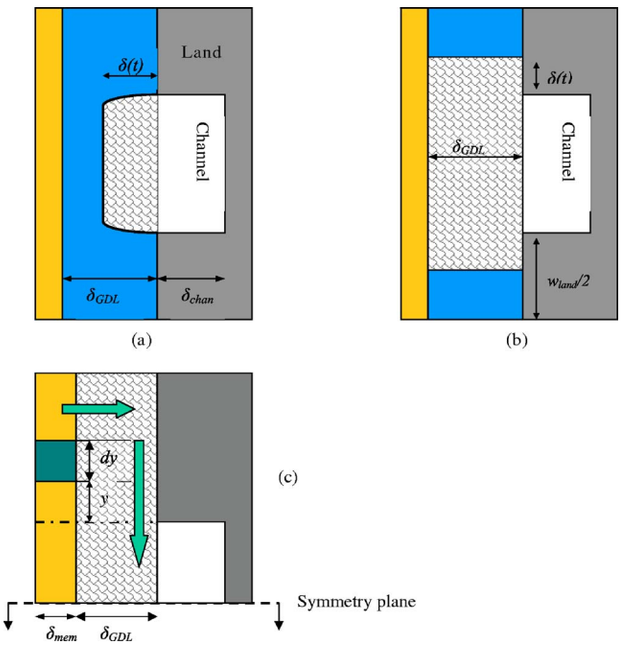

Figure 2. (Color online) Schematic representation of liquid water removal from GDL during: (a) through-plane drying, (b) in-plane drying, and (c) water removal from the land-facing-membrane.

three-dimensional (3D) model for the entire purge process. Finally, the parametric effect of purge conditions on gas purge effectiveness is studied.

Purge Model

Figure 1 schematically depicts physical phenomena involved in gas purge. For clarity, only the cathode side of PEFC is shown. As purge gas is introduced in the gas channel, liquid water in the channel is swept away nearly instantaneously. Subsequently, liquid water in the GDL undergoes evaporation by dry gas flow in the channel (Fig. 1a). GDL drying is characterized by a moving evaporation front that gradually propagates through the GDL. Vapor-phase diffusion dictates the evaporation rate ahead of the front, while capillary transport brings liquid water behind it to the evaporation front. Characteristics of the moving evaporation front in GDL and its numerical treatment were detailed by Luo et al.[32] On completion of GDL drying, water from CL pores and ionomers in CL and membrane starts to be removed by purge gas and the drying front penetrates into CL (Fig. 1b). Gas purge, thus, can be idealized as removal of liquid water present in GDL followed by ionomer drying. In addition, the presence of land and continuous water uptake in purge gas along the flow direction may significantly impact the water removal rate. In order to elucidate these effects, a three-dimensional purge model is developed in the present work. The present model considers the cathode only that encompasses the membrane, cathode GDL, and cathode gas channel. The catalyst layer can be assumed to be an interface between the membrane and GDL because the CL possesses a negligibly small amount of water as far as water removal is concerned. Specifically, a purge model is further divided into GDL drying model and membrane drying model, as to be described below.

GDL drying model.— Following the recent work of Wang and Wang[33] concerning two-phase transients in a PEFC, GDL drying consists of two regimes: through-plane drying followed by in-plane drying, as schematically shown in Fig. 2a and b. In the present work, the analytical model of GDL drying presented by Wang and Wang[33] is extended by coupling the drying front movement with purge gas relative humidity (RH) variation down the channel. RH increase along the channel due to continual evaporation is expected to adversely affect the motion of the drying front in the GDL downstream. Main assumptions used in the model development include:

1. Velocity in the gas channel is constant.
2. The fuel cell remains isothermal during drying due to a much larger heat capacity of cell components than the latent heat of water evaporation.
3. Vapor-phase transport of water in GDL is by diffusion.

Through-plane drying.— As shown in Fig. 2a, at any time instance t, the drying front is at a distance δ away from the GDL-channel interface. The water conservation equation in the GDL can be written as

$$-D_g^{w,eff}\frac{\Delta C}{\delta} = \frac{d}{dt}\left[(\delta_{GDL}-\delta)\frac{\varepsilon s_o \rho_l}{M^{H_2O}}\right] \quad [1]$$

where s_o, ρ_l, and ε stand for the initial liquid saturation in GDL, the density of liquid water and the GDL porosity, respectively. Additionally δ_{GDL} is the GDL thickness, M^{H_2O} the molecular weight of water and $D_g^{w,eff}$ the effective water vapor diffusivity in GDL given by

$$D_g^{w,eff} = D_g^w \varepsilon^n \frac{P_o}{P}\left(\frac{T}{T_o}\right)^{3/2} \quad [2]$$

where n, P_o, and T_o denote the Bruggemann factor for GDL, the reference pressure and temperature, respectively. Assuming the water vapor concentration at the drying front is equal to the saturation value, the concentration gradient, ΔC, can be expressed as

$$\Delta C = C_{sat}(1-\phi) \quad [3]$$

where ϕ is the average RH in gas channel at location x from the channel inlet at time t. Combining Eq. 1-3 and nondimensionalizing the resultant equation yields

$$\frac{1}{Y} = 2\frac{dY}{d\tau}$$

where

$$Y = \frac{\delta}{\delta_{GDL}} \quad \text{and} \quad \tau = \frac{t}{t_1}; \quad t_1 = \frac{\varepsilon s_o \rho_l (\delta_{GDL})^2}{2D_g^{w,eff} M^{H_2O} C_{sat}(1-\phi)} \quad [4]$$

Hence, the solution of Eq. 4 is

$$Y = \sqrt{\tau} \quad [5]$$

Equation 5 shows that through-plane drying at location x along the flow direction is complete when τ becomes the unity. Thus, t_1 can be regarded as the time constant for through-plane drying at location x along the flow direction. As shown in Eq. 5, t_1 depends on gas relative humidity in the channel ϕ, which, in turn, is dependent on time t and location x and can be found by solving the equation of water conservation along the channel

$$\frac{\partial \phi}{\partial t} + u\left(\frac{d\phi}{dx}\right) = \frac{D_g^{w,eff}}{\delta_{chan}} \frac{1-\phi}{\delta} \quad [6]$$

where u is the gas velocity in the channel and δ_{chan} the channel width. Purge gas is commonly fed in the channel at a very high flow rate, and hence, it is safe to neglect the accumulation term in Eq. 6. Combining Eq. 5 and 6 results in

$$u\left(\frac{d\phi}{dx}\right) = \frac{D_g^{w,eff}}{\delta_{chan}} \frac{1-\phi}{\delta_{GDL}} \frac{1}{\sqrt{\tau}} \quad [7]$$

Equation 7 can be solved to obtain RH profile along the gas channel, i.e.

$$\phi = 1 - (1-\phi_{inlet})\left[1 - \frac{\alpha_1 L}{2u} \frac{x^*}{\sqrt{\tau^*}}\right]^2$$

where

$$\alpha_1 = \frac{D_g^{w,eff}}{\delta_{chan}\delta_{GDL}}; \quad x^* = \frac{x}{L}$$

$$\tau^* = \frac{t}{t_1^*}; \quad t_1^* = \frac{\varepsilon s_o \rho_l (\delta_{GDL})^2}{2D_g^{w,eff} M^{H_2O} C_{sat}(1-\phi_{inlet})} \quad [8]$$

where t_1^* is the time constant for through-plane drying at the channel inlet. The above derivation of RH profile in the gas channel is valid for $\phi < 1$. If RH in the channel is unity or larger, then the water flux coming into the channel, given by the right term in Eq. 6, will be zero. Hence, RH variation in the gas channel can be summarized as

$$\phi = 1 - (1-\phi_{inlet})\left[1 - \frac{\alpha_1 L}{2u} \frac{x^*}{\sqrt{\tau^*}}\right]^2 \quad \text{if } \phi < 1$$

$$\frac{\partial \phi}{\partial x} = 0 \quad \text{if } \phi \geq 1 \quad [9]$$

Once the RH profile is obtained, the location of drying front inside GDL at any position along the flow can be expressed as

$$Y(x,t) = Y_{inlet}\sqrt{\frac{1-\phi(x,t)}{1-\phi_{inlet}}} \quad [10]$$

where $Y_{inlet} = \sqrt{\tau^*}$ is the drying front location at the inlet. Physically, Eq. 10 means that liquid water removal diminishes downstream due to water uptake in the purge gas.

In-plane drying.— Figure 2b schematically shows in-plane drying at the cross section at location x along the flow direction. During in-plane drying, the total water flux to the channel consists of evaporative flux from land-facing GDL and diffusive flux from channel-facing dried GDL. Under diffusion, RH across the GDL at the channel-land junction varies from ϕ_1 at the GDL-CL interface to ϕ at the GDL-channel interface. However, in the present work, for simplicity, RH at the channel-land interface is assumed to be equal to ϕ_1. Thus, the following analysis may underpredict the water removal rate. Using a simple resistance network, the total water flux coming into the channel during in-plane drying can be easily shown as

$$\text{Water influx to the channel} \propto 2\frac{1-\phi_1}{\delta}\delta_{GDL} = \frac{\phi_1 - \phi}{\delta_{GDL}} w_{chan} = \frac{1-\phi}{\left[\frac{\delta}{2\delta_{GDL}} + \frac{\delta_{GDL}}{w_{chan}}\right]} \quad [11]$$

where δ is the distance of the drying front from the channel-land junction and w_{chan} is the channel width, respectively. The RH profile in the channel, during in-plane drying, can be obtained similarly to the preceding section, i.e.

$$u\frac{\partial \phi}{\partial x} = \frac{1-\phi}{\left[\frac{\delta w_{chan}}{2(\delta_{GDL})^2} + 1\right]} \frac{D_g^{w,eff}}{\delta_{chan}\delta_{GDL}} \quad [12]$$

The water balance equation in the land region of GDL can be written as

$$-D_g^{w,eff}\frac{C_{sat}(1-\phi_1)}{\delta}\delta_{GDL} = \frac{d}{dt}\left[\left(\frac{w_{land}}{2} - \delta\right)\delta_{GDL}\frac{\varepsilon s_o \rho_l}{M^{H_2O}}\right] \quad [13]$$

where w_{land} is the land width. Combining Eq. 11 and 13 yields

$$-D_g^{w,eff}\frac{C_{sat}(1-\phi)}{\left[\frac{\delta}{\delta_{GDL}} + \frac{2\delta_{GDL}}{w_{chan}}\right]} = \frac{d}{dt}\left[\left(\frac{w_{land}}{2} - \delta\right)\delta_{GDL}\frac{\varepsilon s_o \rho_l}{M^{H_2O}}\right]$$

or

$$2\frac{dX}{d\tau} = \frac{1}{\left[X + \frac{4(\delta_{GDL})^2}{w_{chan}\delta_{land}}\right]} \quad [14]$$

where

$$\tau = \frac{t}{t_2}; \quad t_2 = \frac{\varepsilon s_o \rho_l \left(\frac{\delta_{land}}{2}\right)^2}{2D_g^w M^{H_2O} C_{sat}(1-\phi)}; \quad \text{and} \quad X = \frac{\delta}{\frac{w_{land}}{2}}$$

t_2 can be regarded as the time constant for in-plane drying at location x along the flow direction. Equation 14 can be analytically solved to obtain the drying front location along the in-plane direction within the land region such that

$$X = -\Delta_1 + \sqrt{\Delta_1^2 + \tau} \quad \text{where}$$

$$\Delta_1 = \frac{4(\delta_{GDL})^2}{w_{chan}w_{land}} \quad \text{is a geometric constant} \quad [15]$$

Hence, for complete in-plane drying (i.e., $X = 1$), one has

$$\tau = (1+\Delta_1)^2 - \Delta_1^2 \quad [16]$$

Combining Eq. 12 and Eq. 15

$$u\frac{\partial \phi}{\partial x} = \frac{1-\phi}{\sqrt{1 + \frac{\tau}{\Delta_1^2}}} \frac{D_g^{w,eff}}{\delta_{chan}\delta_{GDL}} \quad [17]$$

For common fuel cell design, $\Delta_1 \sim O(10^{-1})$. Hence, Eq. 17 can be simplified to the following asymptotic forms

Table I. Membrane transport properties.

Property	Correlation	Reference
Membrane water uptake, λ	$\lambda = \begin{cases} [1 + 0.008a^2(T - 303.15)](14a^3 - 19a^2 + 13a) & s = 0 \\ 0.18(T - 273.15) + 9.2 & s > 0 \end{cases}$	Assumed
Proton conductivity, κ	$\kappa = \exp[1455(1/303 - 1/T)]\begin{pmatrix} 0.067a^3 - 0.09a^2 + 0.068a \\ -0.011 \end{pmatrix}$	Tajiri[35]
Note: water activity at the membrane-GDL interface is calculated by $a = C/C_{sat}$ if $s = 0$ $a = [s\rho_l/M^{H_2O} + (1 - s)C_{sat}]/C_{sat}$ if $s > 0$		Pasaogullari and Wang[34]

$$u\frac{\partial \phi}{\partial x} = \frac{D_g^{w,eff}}{\delta_{chan}\delta_{GDL}}(1 - \phi) \quad \text{for} \quad \frac{\tau}{\Delta_1^2} \ll 1$$

$$u\frac{\partial \phi}{\partial x} = \frac{D_g^{w,eff}\Delta_1}{\delta_{chan}\delta_{GDL}}\frac{1 - \phi}{\sqrt{\tau}} \quad \text{for} \quad \frac{\tau}{\Delta_1^2} \gg 1 \qquad [18]$$

These equations can be solved to obtain RH profile in the gas channel during in-plane drying. Subsequently, the drying front location during in-plane drying can be obtained by a procedure similar to the through-plane drying.

Membrane drying model.— Because of different time constants for GDL drying under channel and land region, water content in the membrane portions facing channel and land differs during gas purge. To account for different water content distribution in the in-plane direction, the membrane portions facing channel and land are treated separately under the assumption that there is no in-plane water transport within the membrane. The objective of this submodel is to obtain average membrane water content under channel and land, λ_{chan} and λ_{land}, respectively, as functions of time. Then, the average membrane resistance under channel and land, R_{chan} and R_{land}, at any cross section along the flow direction can be determined by

$$\frac{1}{R_i} = \int_0^{w_i}\int_0^{\delta_{mem}} \frac{1}{\frac{dx}{\kappa(\lambda)}}dy \equiv \frac{\kappa(\lambda_i)w_i}{\delta_{mem}} \quad i = chan, land \qquad [19]$$

where $\kappa(\lambda_i)$ is the average proton conductivity of the membrane facing region i, and w_i the width of region i (i.e., either channel or land). Average HFR at any cross section, HFR_{avg} can be estimated by

$$\frac{w_{cell}}{HFR_{avg}} = \frac{1}{R_{chan}} + \frac{1}{R_{land}}$$

Adding contact resistance into the total HFR value, one has

$$HFR = HFR_{avg} + R_{contact} \qquad [20]$$

The computation of membrane water content during gas purge can be divided into the following three stages:

Stage 1. Through-plane drying.— Liquid water is always present at the GDL-CL interface (CL is assumed to be an interface between GDL and membrane) during through-plane drying. In the present work, the average water saturation under channel and land is used to obtain water activity at the membrane-CL interface. Using membrane water uptake curve, λ_{chan} and λ_{land} are computed, and, in turn, are used to obtain membrane proton conductivity. For following calculations the Gore-Select membrane is used, whose properties are listed in Table I.

Stage 2. In-plane drying.— During in-plane drying, a certain fraction of the membrane facing the land is in contact with liquid water, giving rise to much higher proton conductivity compared to the "dry" portion under the land. Using resistance network analogy, it can be readily shown that average HFR value is controlled by the proton conductivity of the "wet" portion. Hence, the average membrane ionic conductivity under the land can be assumed to be given by $\kappa_{avg}^{land} = \kappa(s_{avg}^{land})$ in the same manner as in stage 1. Here, water content in the membrane portion facing the channel can be obtained as follows

$$\frac{\rho_{dry}\delta_{mem}}{EW}\frac{\partial \lambda_{chan}}{\partial t} = -D_g^{w,eff}\frac{P_{sat}}{RT}\frac{(a_{chan} - \phi)}{\delta_{GDL}} \qquad [21]$$

where ρ_{dry} and EW represent the density of a dry membrane and its equivalent weight respectively, a_{chan} the water activity at the GDL-membrane interface facing channel and ϕ the RH in the gas channel. Physically, Eq. 21 expresses the drying rate of the channel-facing membrane owing to vapor diffusion across the GDL. Using water uptake of the membrane, Eq. 21 can be further expressed as

$$\left(\frac{d\lambda}{da}\right)\frac{\partial a_{chan}}{\partial t} = -\chi_1(a_{chan} - \phi)$$

where

$$\chi_1 = D_g^{w,eff}\frac{P_{sat}}{RT}\frac{EW}{\rho_{dry}\delta_{mem}\delta_{GDL}} \qquad [22]$$

Stage 3. Vapor-phase transport.— After in-plane drying is complete, water removal from the membrane is driven by the vapor concentration gradient across GDL. For simplicity, water activity at the membrane surface facing the land is assumed to be uniform along the in-plane direction and is given by a_{land}. The water vapor flux from a differential element dy at a distance y from the channel-land interface, as shown in Fig. 2c, is given by

$$d\dot{m}_w = D_g^{w,eff}\frac{P_{sat}}{RT}\frac{(a_{land} - \phi)}{d\delta_{diff}}dy \qquad [23]$$

where $d\delta_{diff}$ is the effective diffusion length for the differential element. Simplifying $d\delta_{diff}$ as $(\delta_{GDL} + y)$, the water vapor flux can be expressed as

$$d\dot{m}_w = D_g^{w,eff}\frac{P_{sat}}{RT}\frac{(a_{land} - \phi)}{(\delta_{GDL} + y)}dy \qquad [24]$$

The total water vapor flux from the membrane under the land can be obtained by integrating Eq. 24 over land width

$$\dot{m}_w = D_g^{w,eff}\frac{P_{sat}}{RT}\frac{(a_{land} - \phi)}{\delta_{eff}}w_{land}$$

$$= 2 \times \int_0^{\frac{w_{land}}{2}} D_g^{w,eff}\frac{P_{sat}}{RT}\frac{(a_{land} - \phi)}{(\delta_{GDL} + y)}dy$$

Hence

$$\delta_{eff} = \frac{\delta_{land}}{2\ln\left(1 + \frac{w_{land}}{2\delta_{GDL}}\right)} \qquad [25]$$

Writing water conservation in the land-facing membrane gives

Table II. Geometrical parameters and purge conditions.

Parameter	Value
GDL thickness, δ_{GDL}	230 μm
GDL porosity, ε	0.6
Bruggemann factor, n	2
Membrane thickness, δ_{mem}	30 μm
Cell length, L	54 mm
Channel width, w	0.5 mm
Channel depth, δ_{chan}	1.0 mm
Land width	0.5 mm
Purge conditions	
Purge gas	N_2
Cell temperature	55°C
Inlet RH, ϕ_{inlet}	0.4
Flow rate	3.74×10^{-6} m^3/s (4.48 L/min for a 25 cm^2 cell with parallel flow field)

$$\frac{\rho_{dry}\delta_{mem}}{EW}\frac{\partial \lambda_{land}}{\partial t} = -D_g^{w,eff}\frac{P_{sat}}{RT}\frac{(a_{land}-\phi)}{\delta_{eff}} \quad [26]$$

Using analysis similar to stage 2

$$\left(\frac{d\lambda}{da}\right)\frac{\partial a_{land}}{\partial t} = -\chi_2(a_{land}-\phi)$$

$$\chi_2 = D_g^{w,eff}\frac{P_{sat}}{RT}\frac{EW}{\rho_{dry}\delta_{mem}\delta_{eff}} \quad [27]$$

Because there is no liquid water present during stage 3, it is assumed that the water influx to the channel is small. Consequently, the RH in gas channel remains constant at the inlet RH value during stage 3, provided that purge gas flow rate is sufficiently high. Therefore, Eq. 22 and Eq. 27 are solved with substituting ϕ with ϕ_{inlet} to obtain λ_{chan} and λ_{land}, respectively, as function of time.

Results and Discussion

The geometric parameters and purge conditions used in the present study are summarized in Table II. The purge conditions mentioned in Table II will be regarded as base case parameters in the following discussion. The gas flow rate mentioned in Table II is equivalent to 4.48 L/min flow rate in a fuel cell with 25 cm^2 active area and parallel flowfield, assuming that flow is distributed uniformly in each channel. In the following, the flow rate will always be referred to that in the 25 cm^2 fuel cell. Detailed numerical simulations of PEFC operation under common prepurge conditions show an average GDL liquid saturation in the range of 10–20%. Therefore, for the present work an initial GDL liquid saturation is assumed to be 16%.

Figure 3 shows the gas channel RH variation along the flow direction. The evaporation flux to the channel is inversely proportional to the distance of the drying front from the GDL-channel interface; hence, RH rises rapidly to unity at the beginning of gas purge. As the drying front further invades the GDL, the water flux diminishes, resulting in subsequent decrease in RH along the channel. Higher RH toward the channel exit, as displayed in Fig. 3, curtails the water removal capacity of purge gas and thus is expected to significantly delay GDL drying time along the flow direction. Figure 4 shows the variation of average liquid water saturation in the GDL as a function of square root of purge time at inlet ($x = 0$), middle ($x = 0.5$), and outlet location ($x = 1$). It is observed that the GDL drying time constant varies from 29 s to 36 s along the channel length. At each location, variation in the slope represents the transition from through-plane to in-plane drying stage. Smaller slope during in-plane drying is indicative of the difficulty to remove liquid water under the land.

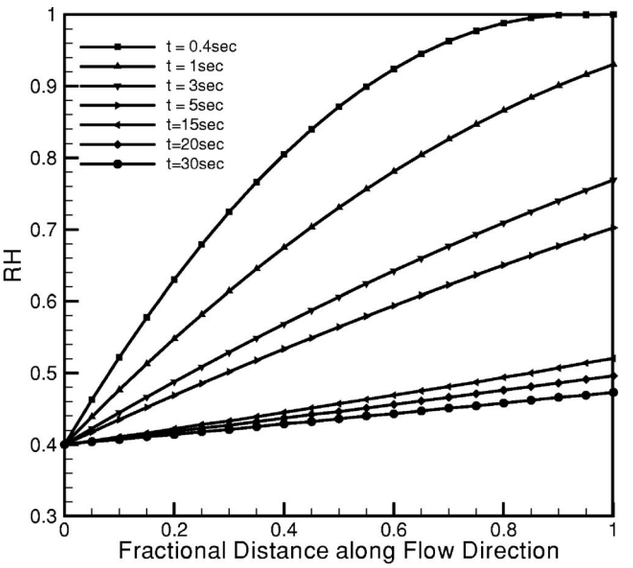

Figure 3. RH variation in gas channel for gas purge with 4.48 L/min flow rate and 40% inlet RH at 55°C cell temperature.

Figure 5 shows the HFR variation with purge time at the three representative locations along the flow. HFR variation at any location can be divided into four different regimes, as marked in Fig. 5 for the inlet location as an example. During through-plane drying (i.e., regime A), the drying front penetrates the GDL, but the membrane surface, both facing the channel and land, does not feel the influence of drying; as such, there is a very little increase in HFR. At the end of regime A, water activity at the membrane surface facing the channel becomes unity. Regime B, the in-plane drying stage, is characterized by a faster HFR increase rate followed by significantly smaller HFR increase rate. Rapid drying of the channel-facing membrane due to vapor transport governs the average HFR value in the initial stage of regime B. With time, water activity at the GDL-membrane interface facing channel asymptotically decreases to the RH of purge gas, limiting the contribution of channel-facing mem-

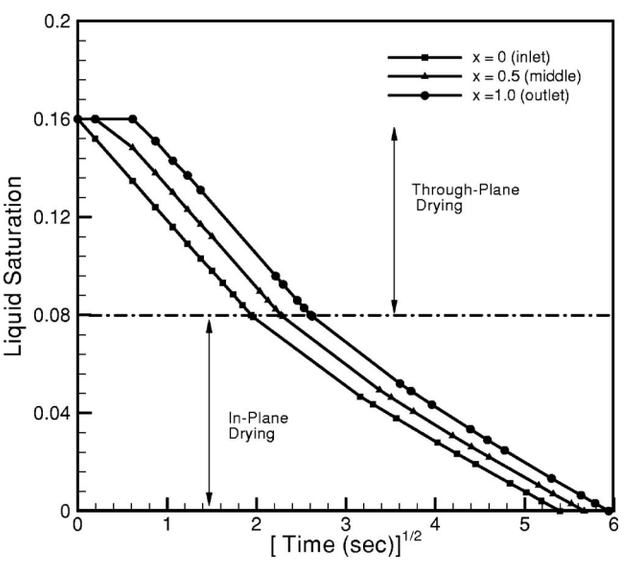

Figure 4. Variation of average liquid saturation in GDL with purge time for gas purge with 4.48 L/min flow rate and 40% inlet RH at 55°C cell temperature.

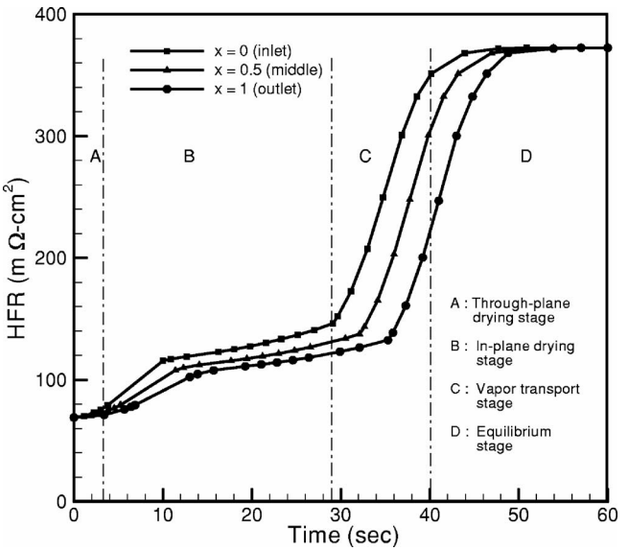

Figure 5. HFR variation with purge time for gas purge with 4.48 L/min flow rate and 40% inlet RH at 55°C cell temperature.

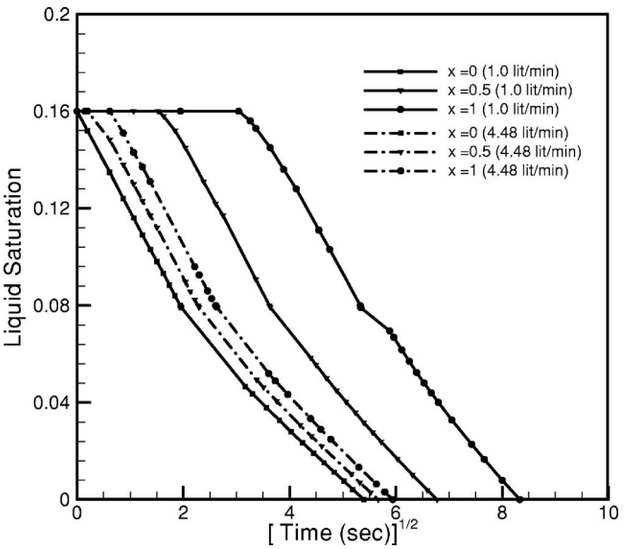

Figure 7. Variation of average liquid saturation in GDL with purge time for gas purge with 1.0 L/min flow rate and 40% inlet RH at 55°C cell temperature.

brane drying to the average HFR value. Further increase in the HFR thus arises from the GDL desaturation under the land, furnishing significantly smaller slope to the HFR variation. Although in the present analysis, HFR increase in the land-facing membrane is correlated with average liquid saturation under the land portion and is thus underpredicted, it is expected that more rigorous analysis would not change the characteristics of stage B. After complete drying, sharp increase in HFR, as displayed in stage C of Fig. 5, can be largely attributed to the land-facing membrane drying due to water vapor transport. The asymptotic decrease in the water activity at the membrane-GDL interface to the RH in the gas channel decays the rate of HFR increase toward the end of stage C. Thereafter, no significant increase in HFR is possible, as observed in equilibrium stage, stage D. Similar to GDL drying, time constants of these four stages increase along the flow direction, as shown in Fig. 5.

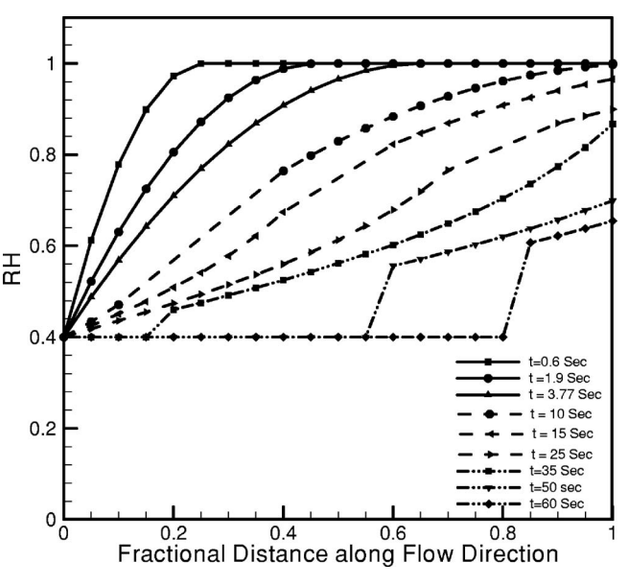

Figure 6. RH variation in gas channel for gas purge with 1.0 L/min flow rate and 40% inlet RH at 55°C cell temperature.

The above-described variations along the flow direction become more prominent at smaller gas flow rates. Figure 6 shows the gas channel RH variation along flow direction for 1.0 L/min purge gas flow rate while keeping the other parameters the same. Smaller gas flow rate decreases the water removal rate from the channel and thereby renders a larger increase in RH along the flow direction, as displayed in Fig. 6. It is found that for 1.0 L/min flow rate, through-plane drying time constant varies from 3.77 s at the inlet to 28.4 s at the outlet location. Therefore, during 3.77 s $< t <$ 28.4 s, both in-plane drying and through-plane drying regimes coexist along the channel length. The water influx to the channel during in-plane drying is significantly smaller than during through-plane drying, which renders a convex-shaped RH profile for the cell length under in-plane drying regime and a concave-shaped RH profile for the remaining cell length. The point of inflection in the RH profile indicates the location of complete through-plane drying along the channel length, as shown by RH profiles for t = 10 s, 15 s, and 25 s in Fig. 6. Water vapor removal after complete GDL desaturation furnishes very little increase to the channel RH. Hence, the flat portion of RH profiles for 35 s $\leq t \leq$ 60 s, shown in Fig. 6, represents the dry fraction of cell length.

Figure 7 depicts the variation of liquid water saturation as a function of square root of purge time at the three representative locations along the flow. The fact that the time constant for liquid water removal remains the same at the inlet section but differs significantly along the channel length for 1.0 L/min and 4.48 L/min purge gas flow rates, as shown in Fig. 7, underpins the need to account for the flow direction to elucidate gas purge characteristics. Figure 8 shows the variation of outlet RH with purge time for 4.48 L/min and 1.0 L/min. Significantly higher outlet RH is easily expected for the low gas flow rate. However, as displayed in Fig. 8, after complete GDL desaturation, outlet RH sharply recovers to the inlet RH value for both flow rates. Figure 9 shows the corresponding HFR variations with purge time at the three representative locations along the flow.

Figure 10 shows the effect of cell temperature on purge effectiveness while keeping the other parameters the same as the base case. As shown in Fig. 10, the drying time constant decreases appreciably with cell temperature. The saturated water vapor concentration, hence, the evaporation rate, increases significantly with the cell temperature, resulting in a smaller drying time constant. It should be mentioned that in the present work capillary transport of

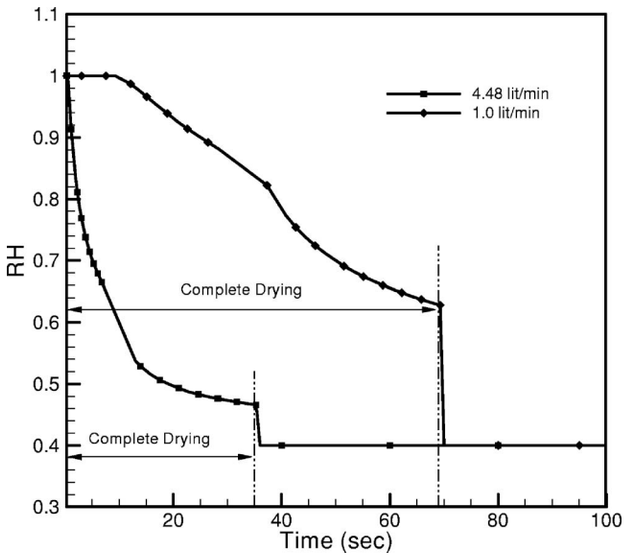

Figure 8. Variation of outlet RH with purge time for 4.48 L/min and 1.0 L/min purge gas flow rate with 40% inlet RH at 55°C cell temperature.

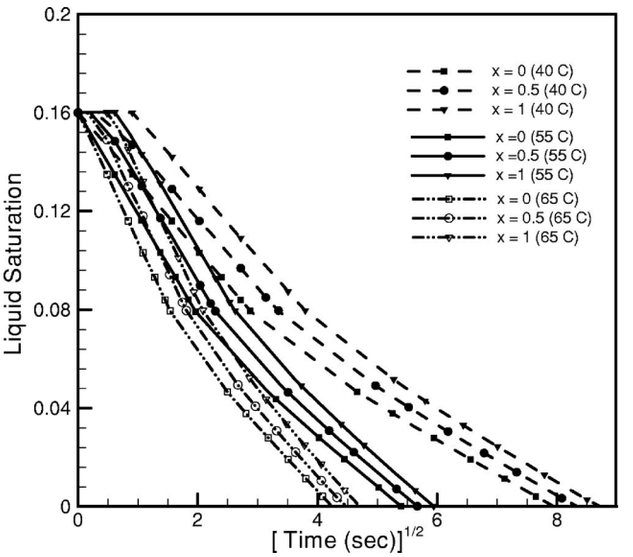

Figure 10. Variation of average liquid saturation in GDL with purge time for different cell temperatures during gas purge.

liquid water from deep inside GDL to the drying front is not taken into account. Physically, drying front movement in GDL is governed by the relative magnitude of vapor transport ahead of the drying front and liquid water transport behind the drying front. At lower temperatures, vapor transport from the drying front to the channel slows down and the relative importance of capillary transport of liquid water to the drying front substantially increases in determining the drying time constant. The present analysis, therefore, overpredicts the drying time constants, especially at lower temperatures. Figure 11a and b shows corresponding HFR variations along the flow direction. The difference in the maximum HFR value is due to the dependence of membrane protonic conductivity on temperature.

Figure 12 shows the effect of inlet RH on the GDL drying rate. Low inlet RH provides larger water vapor concentration gradient between the drying front and channel, and thus lowers the drying time constant, as shown in Fig. 12. Figure 13 displays the reduction in membrane water content as a function of time for 0% and 40% inlet RH. Initially, the membrane, equilibrated with liquid water, has a water content of 19.2 (moles of water per mole of SO_3^-) that subsequently decreases with GDL drying. The rate of membrane drying increases significantly after the completion of GDL desaturation. As shown in Fig. 13, inlet gas channel RH dictates the lowest possible membrane water content in a gas purge, therefore, a dry purge gas favors effective purge because it not only lowers the drying time constant but also provides a larger driving force for membrane drying.

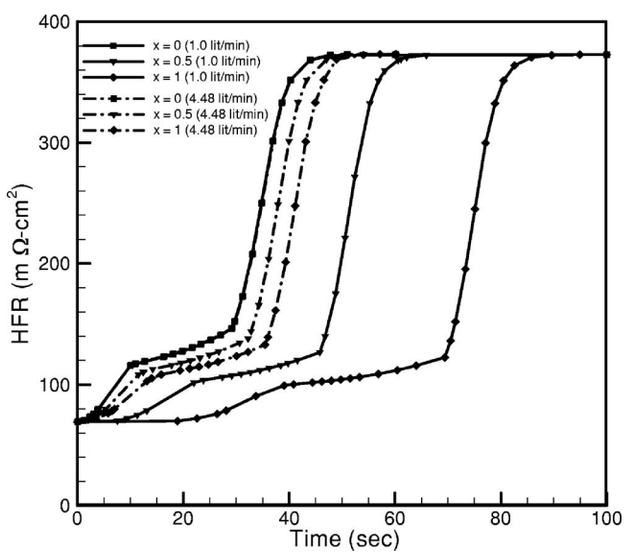

Figure 9. HFR variation with purge time for gas purge with 1.0 L/min flow rate and 40% inlet RH at 55°C cell temperature.

It is instructive to compare the time constant of complete GDL drying predicted by the present purge theory with an earlier measurement by X-ray microtomography.[9] Figure 14 plots the time constant as a function of the initial liquid water saturation in GDL under two cell temperatures with dry purge gas and extremely large flow rate characteristics of a differential cell. As can be seen, the predicted total drying time constant (8.8 min) for 100% initial GDL saturation and 20°C cell temperature agrees well with the X-ray microtomographic experiments[9] (~10–12 min) conducted under the same conditions. Figure 14 further shows that for a realistic fuel cell purged at 55°C and with a very large flow rate, gas purge must be conducted for at least 20 s to remove liquid water completely from a PEFC. In practice, the purge time could be substantially extended if the gas flow rate is moderate. Figure 14 also indicates significantly longer purge time at lower purge temperature, underscoring the fundamental difficulty in removing residual water when a PEFC engine remains at low temperatures at shutdown, e.g., after short trips.

Conclusion

A fundamental understanding of gas purge mechanisms is essential to establish effective and energy-saving gas purge protocols. In the present work, a purge model elucidating underlying physical phenomena in gas purge is presented. It is found that at a cross section along the flow direction, GDL drying consists of through-plane drying followed by in-plane drying with larger time constant due to the difficulty to remove liquid water under the land. Membrane HFR variation during gas purge is characterized into four stages: through-plane drying, in-plane drying, a vapor transport stage that provides significantly higher rate of HFR increase, followed by an equilibrium stage. The predicted drying time constant is found to be in good agreement with the tomographic data reported previously in the literature. Additionally, it is seen that the drying time constants and the membrane HFR vary substantially along the

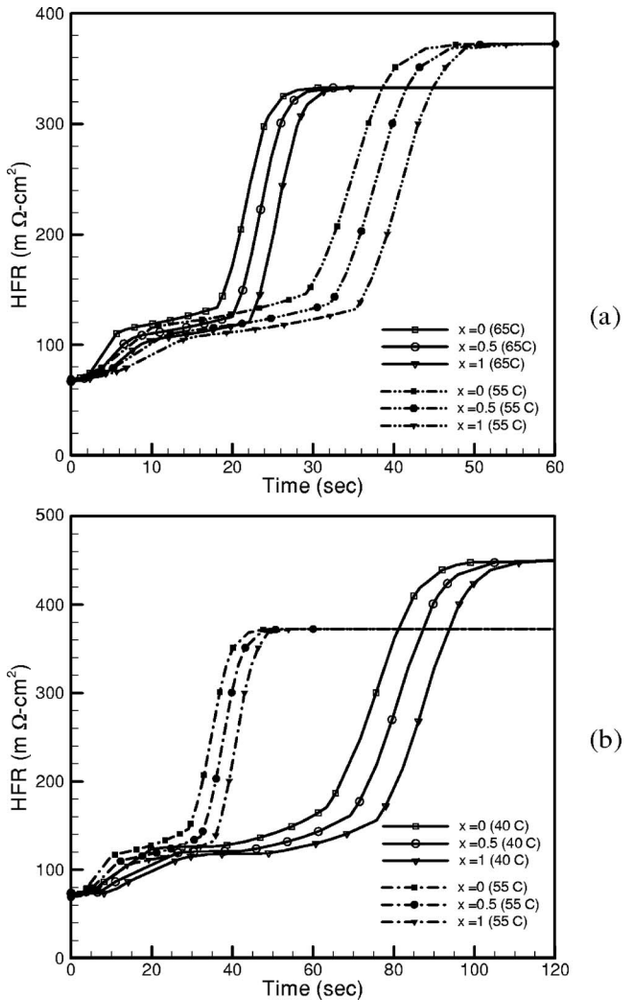

Figure 11. HFR variation with purge time for: (a) 65°C cell temperature and (b) 40°C cell temperature. HFR variations for 55°C cell temperature are shown as dashed lines.

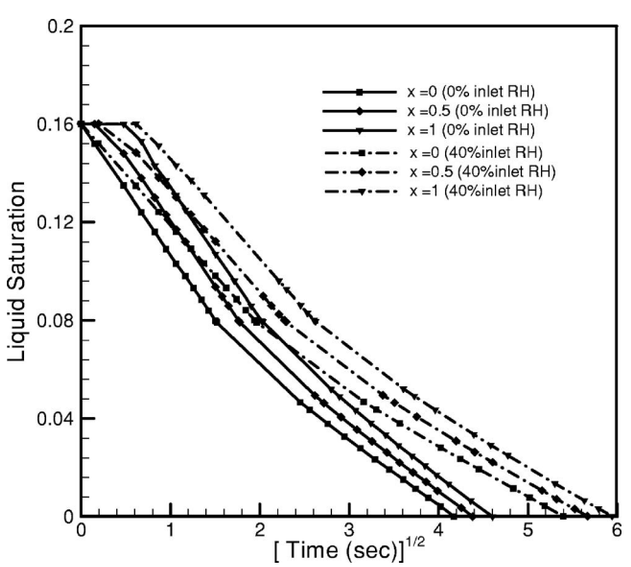

Figure 12. Variation of average liquid saturation in GDL with purge time for various gas purge inlet RH with 4.48 L/min flow rate at 55°C cell temperature.

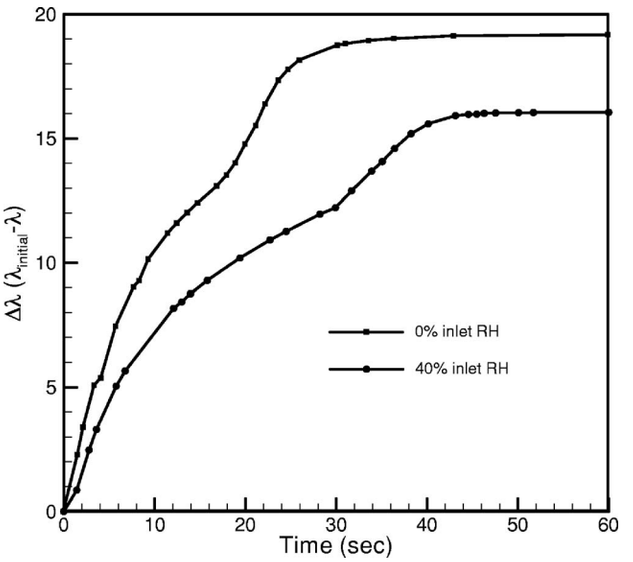

Figure 13. Increase in membrane water storage capacity as function of purge time for 0% and 40% inlet RH. Initial water content is same for both cases and equal to 19.2.

flow, underpinning the need to account for the three-dimensional effects in the description of gas purge. The effect of purge conditions on the purge effectiveness is investigated, and it is found that high gas flow rate, high cell temperature, and dry purge gas favor effective purge.

Although the present model elucidates fundamental characteristics of gas purge, it does not account for the liquid water transport from GDL and CL to the drying front. Efforts are underway to develop a more rigorous purge model, based on computational fluid dynamics that incorporates detailed two-phase flow in GDL and CL behind the evaporation front with an exhaustive treatment of water removal from the ionomer phase in CL and membrane. In parallel,

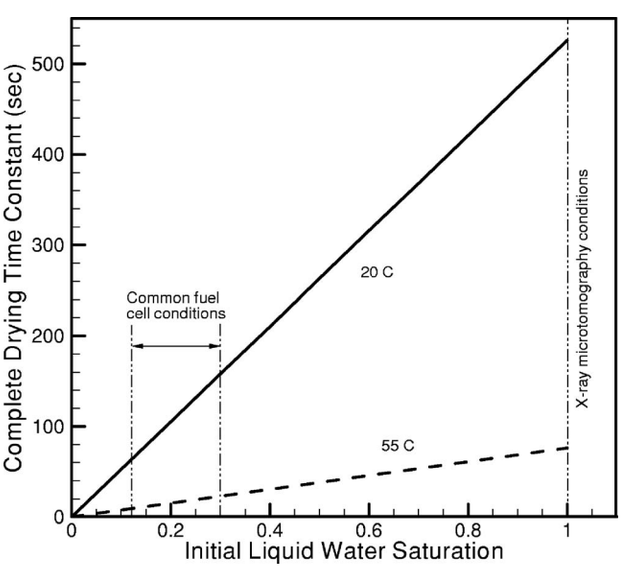

Figure 14. Variation of drying time constant as a function of initial liquid water saturation in GDL with dry purge gas and very large flow rate characteristic of a differential cell (i.e., in X-ray microtomographic experiments[9]). The predicted total drying time constant at 20°C (8.8 min) agrees well with the tomographic data (~10–12 min).

experimental characterization of the purge curve as shown in Fig. 5 and detailed validation of the present purge model are ongoing and shall be reported in a future publication.

Acknowledgments

Financial support for this work by Nissan Motor Company Limited is gratefully acknowledged. The authors thank fruitful discussions with Y. Tabuchi.

The Pennsylvania State University assisted in meeting the publication costs of this article.

List of Symbols

a	water activity
C	water concentration, mol/m^3
D_g	vapor diffusivity, m^2/s
EW	equivalent weight of polymer membrane, kg/mol
L	channel length, m
$\dot{m}_w$	water vapor flux, mol/s
M^{H_2O}	molecular weight of water, kg/mol
n	Bruggemann factor
P_{sat}	saturated vapor pressure, Pa
R	universal gas constant, 8.314 J/mol K
R_i	membrane ionic resistance facing i, i = channel, land, Ω
$R_{contact}$	contact resistance, Ω m^2
s	liquid water saturation
t	time, s
T	temperature, K
u	velocity in gas channel, m/s
w	width, m

Greek

ε	porosity
λ	membrane water content
κ	membrane ionic conductivity S/m
ϕ	relative humidity
ρ	density, kg/m^3
ρ_{dry}	density of dry membrane, kg/m^3
δ	thickness, m

Subscripts

avg	average
chan	gas channel
GDL	gas diffusion layer
inlet	inlet location
l	liquid water
land	land
o	initial value
sat	saturation

Superscripts

eff	effective
w	water

References

1. M. Oszcipok, D. Riemann, U. Kronenwett, M. Kreideweis, and M. Zedda, *J. Power Sources*, **145**, 407 (2005).
2. L. Mao and C. Y. Wang, *J. Electrochem. Soc.*, **154**, B139 (2007).
3. L. Mao, C. Y. Wang, and Y. Tabuchi, *J. Electrochem. Soc.*, **154**, B341 (2007).
4. K. Tajiri, Y. Tabuchi, and C. Y. Wang, *J. Electrochem. Soc.*, **154**, B147 (2007).
5. S. Ge and C. Y. Wang, *Electrochem. Solid-State Lett.*, **9**, A499 (2006).
6. S. Ge and C. Y. Wang, *Electrochim. Acta*, **52**, 4825 (2007).
7. J. Hou, H. Yu, B. Yi, Y. Xiao, H. Wang, S. Sun, and P. Ming, *Electrochem. Solid-State Lett.*, **10**, B11 (2007).
8. R. Bradean, H. Haas, A. Desousa, R. Rahmani, K. Fong, K. Eggen, D. Ayotte, A. Roett, and A. Huang, Paper presented at AIChE 2005 Annual Meeting, Cincinnati, OH, Oct 30–Nov. 4, 2005.
9. P. K. Sinha, P. Halleck, and C. Y. Wang, *Electrochem. Solid-State Lett.*, **9**, A344 (2006).
10. M. Prat, *Int. J. Multiphase Flow*, **19**(4), 691 (1993).
11. M. Prat, *Int. J. Multiphase Flow*, **21**(5), 875 (1995).
12. J. B. Laurindo and M. Prat, *Chem. Eng. Sci.*, **51**, 5171 (1996).
13. Y. L. Bray and M. Prat, *Int. J. Heat Mass Transfer*, **42**, 4207 (1999).
14. A. G. Yortsos, A. K. Stubos, A. G. Boudouvis, and Y. C. Yortsos, *Adv. Water Resour.*, **24**, 439 (2001).
15. A. G. Yortsos, A. G. Boudouvis, A. K. Stubos, I. N. Tsimpanogiannis, and Y. C. Yortsos, *Phys. Rev. E*, **68**, 037303 (2003).
16. A. G. Yortsos, A. G. Boudouvis, A. K. Stubos, I. N. Tsimpanogiannis, and Y. C. Yortsos, *AIChE J.*, **50**, 2721 (2004).
17. L. A. Segura and P. G. Toledo, *Lat. Am. Appl. Res.*, **35**, 43 (2005).
18. A. V. Luikov, *Int. J. Heat Mass Transfer*, **18**, 1 (1975).
19. S. Whitaker, *Adv. Heat Transfer*, **13**, 119 (1977).
20. O. A. Plumb, G. A. Spolek, and B. A. Olmstead, *Int. J. Heat Mass Transfer*, **28**, 1669 (1985).
21. M. Ilic and I. W. Turner, *Appl. Math. Model.*, **10**, 16 (1986).
22. M. Ilic and I. W. Turner, *Int. J. Heat Mass Transfer*, **32**, 2351 (1989).
23. S. B. Nasrallah and P. Perre, *Int. J. Heat Mass Transfer*, **31**, 957 (1988).
24. M. Quintard and S. Whitaker, *Adv. Heat Transfer*, **28**, 369 (1993).
25. J. A. Rogers and M. Kaviany, *Int. J. Heat Mass Transfer*, **35**, 469 (1992).
26. W. T. H. Chou and S. Whitaker, *Drying Technol.*, **1**, 3 (1983).
27. M. Kaviany and M. Mittal, *Int. J. Heat Mass Transfer*, **30**, 1407 (1987).
28. C. L. D. Huang, *Int. J. Heat Mass Transfer*, **22**, 1295 (1979).
29. M. G. Goyeneche, D. Lasseux, and D. Bruneau, *Transp. Porous Media*, **48**, 125 (2002).
30. T. Lu, P. Jiang, and S. Shen, *Heat Mass Transfer*, **41**, 1103 (2005).
31. N Shahidzadeh-Bonn, A. Azouni, and P. Coussot, *J. Phys.: Condens. Matter*, **19**, 112101 (2007).
32. G. Luo, H. Ju, and C. Y. Wang, *J. Electrochem. Soc.*, **154**, B316 (2007).
33. Y. Wang and C. Y. Wang, *J. Electrochem. Soc.*, **154**, B636 (2007).
34. U. Pasaogullari and C. Y. Wang, *J. Electrochem. Soc.*, **152**, A380 (2005).
35. K. Tajiri, Personal communications, 2006.